

Supporting information for

**Operando Generated Ordered Heterogeneous Catalyst for the
Selective Conversion of CO₂ to Methanol**

**Arjun Cherevotan,^{1,2} Jithu Raj,^{1,2#} Lakshay Dheer,^{2,3,4#} Soumyabrata
Roy,^{1,2§} Shreya Sarkar,^{1,2} Risov Das,^{1,2} Chathakudath P. Vinod,⁵ Shaojun
Xu,^{6,7} Peter Wells,^{6,8,9} Umesh V. Waghmare^{2,3} and Sebastian C. Peter^{1,2*}**

¹*New Chemistry Unit, Jawaharlal Nehru Centre for Advanced Scientific Research, Jakkur,
Bangalore-560064*

²*School of Advanced Materials, Jawaharlal Nehru Centre for Advanced Scientific Research,
Jakkur, Bangalore-560064*

³*Theoretical Sciences Unit, Jawaharlal Nehru Centre for Advanced Scientific Research,
Jakkur, Bangalore-560064*

⁴*Chemistry and Physics of Materials Unit, Jawaharlal Nehru Centre for Advanced Scientific
Research, Jakkur, Bangalore-560064*

⁵*Catalysis and Inorganic Chemistry Division, National Chemical laboratory, Dr. Homi
Bhabha Road, Pune, 410008*

⁶*UK Catalysis Hub, Research Complex at Harwell, Didcot, OX11 0FA, UK*

⁷*Cardiff Catalysis Institute, School of Chemistry, Cardiff University, Cardiff, CF10 3AT, UK*

⁸*School of Chemistry, University of Southampton, Southampton, UK*

⁹*Diamond Light Source, Didcot, UK*

*Corresponding author. Phone: 080-22082998, Fax: 080-22082627

sebastiancp@jncasr.ac.in (S. C. Peter)

#Equally Contributed

§Present Address: *Department of Materials Science and Nanoengineering, Rice University,
Houston, TX, United States*

S1. Experimental Sections:

1.1. Materials:

Tetraethyl orthosilicate (TEOS) (>99% GC, Sigma Aldrich), pluronic P123 ($M_n \sim 5800$, Sigma Aldrich), HNO_3 (69% analytical grade, Merck Chemicals), H_2SO_4 (98% analytical grade, Merck Chemicals), nickel nitrate hexahydrate (98%, SDFCL) and indium nitrate hydrate (99.99%, Sigma Aldrich).

1.2. Synthesis:

SBA-15: The support material Santa Barbara Amorphous (SBA-15)¹ was synthesized by modifying an already reported method.² Four grams of Pluronic P123 was dissolved in 105 mL of deionized water and 10.8 mL of 98% H_2SO_4 to act as a soft template. Then 9.063 mL of TEOS was added to the solution with high rate of stirring for 3.5 hours at 313 K, followed by hydrothermal treatment at 373 K for 30 hours. The obtained white powder was filtered, washed with deionized water, and dried at 373 K overnight. Lastly it was calcined for 6 hours at 823 K.

Ni-In/SBA-15: A typical method of incipient wetness impregnation was followed with slight modification to distribute Ni-In system on SBA-15.^{3, 4} Ni(II) and In(III) nitrates were dissolved in 4 M HNO_3 solution. The nitrate salts were weighed so as to get 23% of metal loading with different ratio of Ni:In – 3:1 (Ni-In/SBA-15-a), 2:1 (Ni-In/SBA-15-b), 1:1 (Ni-In/SBA-15-c) and 7:3 (Ni-In/SBA-15-d). SBA-15 was soaked in the solution for an hour, which propels the solution impregnation into the channels by capillary action. The excess solution was dried at 333 K in fume hood and further in vacuum oven at 393 K overnight. The precursor was reduced at 1083 K under H_2 flow (**Figure 1**). The controlled catalyst (without In) Ni/SBA-15 was synthesized by following same steps. The $\text{NiO-In}_2\text{O}_3/\text{SBA-15}$ was synthesized by oxidizing Ni-In/SBA-15-d at 773 K for 5 hours under air.

Interestingly, identical features were observed in the XRD patterns of all the aforementioned combinations of Ni-In (NiIn , Ni_2In , Ni_3In and Ni_7In_3) phases on SBA-15

regardless of the ratio of metal precursor solution (**Figure S1**), which confirm the formation of triclinic Ni_7In_3 IMC phase having space group $P\bar{1}$. Among the four phases, $\text{Ni}_7\text{In}_3/\text{SBA-15}$ was found to form in the pure targeted phase up to the XRD detection limits (**Figure S1 and S2b**). On the other hand, peaks at 41.6° and 48.5° corresponding to Ni_3In IMC (SG: $Pm\bar{3}m$) occurred as a minor impurity alongside the major Ni_7In_3 phase obtained in $\text{Ni}_3\text{In}/\text{SBA-15}$ (**Figure S2**) synthesis. The other targeted phases $\text{Ni}_3\text{In}/\text{SBA-15}$ and $\text{Ni}_2\text{In}/\text{SBA-15}$ lead to the formation of Ni ($Fm\bar{3}m$) as a minor phase along with Ni_7In_3 as the major phase.

1.3. Material Characterization:

The phase formation on SBA-15 was confirmed by X-ray diffraction (XRD) collected on PANalytical X-ray diffractometer with $\text{Cu K}\alpha$ radiation at 45 kV and 40 mA. The features of the PXRD patterns were compared with simulated pattern from Pearson Database. The adsorption isotherms were studied by using N_2 at 77 K on BelCat instrument. Prior to the measurements the powders were treated for degassing at 423 K for 6 hours. The specific surface area was confirmed by Brunaur-Emmett-Teller (BET) method and pore size distribution by classical BJH (Barrett, Joyner and Halenda) method. TEM images and selected area electron diffraction patterns were collected using a JEOL JEM-2010 TEM instrument and color mapping was done in TECHNAI. The samples for these measurements were prepared by sonicating the nanocrystalline powders in ethanol and drop-casting a small volume onto a carbon-coated copper grid.

The TEM and SEM micrographs of SBA-15 visualize the separated hexagonal channels of the mesoporous support (**Figure S2c and Figure S3a**). The TEM images for both $\text{Ni}/\text{SBA-15}$ and $\text{Ni}_7\text{In}_3/\text{SBA-15}$ were indistinguishable due to extensive distribution of metal/IM nanoparticles (NPs) over the channels of SBA-15 (**Figure S2d and Figure S4**). STEM color mapping on the NPs of $\text{Ni}_7\text{In}_3/\text{SBA-15}$ shows the uniform elemental

distribution of Ni and In all over the spherical nanoparticles confirming the formation of the IMC (**Figure S3c**), which is well complemented by the SEM images (**Figure S3b**). The average particle size in the case of Ni₇In₃ was found to be 7.7 nm (**Figure S2e**).

The N₂ adsorption-desorption experiment exhibits type IV isotherm (Brunauer definition) with hysteresis loop (**Figure S2f**), typical of hexagonal and cylindrical mesoporous materials.⁵ There is a fast increase in adsorption volume between 0.6-0.8 p/p₀ which is indicative of capillary condensation attributed to the pre-formation of N₂ on the pore walls due to multilayer adsorption.⁶ Ni/SBA-15 and Ni₇In₃/SBA-15 samples, exhibited a left-shift of the sharp rise in the adsorption isotherms and drastically diminished surface areas [from 675 m²/g (SBA-15) to 290 m²/g (Ni/SBA-15) and 265 m²/g (Ni₇In₃/SBA-15)]. This lowering of surface area concludes that impregnated Ni and Ni₇In₃ clusters decreases the N₂ probing surface inside the mesopores.⁷ Additionally, the decrease in pore size upon the impregnation further confirms the formation Ni metal and Ni₇In₃ IMC as nanoparticles within the channels of mesoporous SBA-15 (**Figure S2g**).

1.4. Catalyst Extrusion:

Wire type extrudates were used for the tubular reactor. A paste was made from catalyst powder by grinding 5 g of it with 1.5 g of pseudoboehmite (AlO(OH)) and 10 mL of 0.5 M HNO₃. This was then passed through a manually operated wire profiled die to get a wire of 0.5 mm diameter and 1 mm length. The extrudates were dried in atmospheric conditions and then calcined overnight at 373 K to make it strong. The extrudates were crushed and characterized by XRD.

1.5. Catalyst Screening Test:

The efficiency of the catalysts towards CO₂ reduction was screened by a fixed bed vapor phase down flow reactor having a bed volume of 9.2 cm³. Two flow rates were used, that is,

40 NLPH (1CO₂:3H₂) and 50 NLPH (1CO₂:4H₂). The reactions were performed at 523 K and 573 K, also at different pressures, that is, ambient to 50 bar. The catalyst after loading was activated by passing 5:10 mixture of H₂ and N₂ at 673 K. The gases were analyzed in real time by Agilent GC 7890B, with TCD and FID as the detector. The liquid products were condensed by chiller and analysis by FID after 15 hours of reaction. N₂ and isopropyl alcohol (IPA) were used as the internal standards for gas and liquid analysis, respectively.

1.6. X-ray Photoelectron Spectroscopy (XPS):

XPS measurements were carried out using Thermo K-alpha+ spectrometer using micro focused and monochromated Al K α radiation with energy 1486.6 eV. The pass energy for spectral acquisition was kept at 50 eV for individual core-levels. The electron flood gun was utilized for providing charge compensation during data acquisition. Further, the individual core-level spectra were checked for charging using C1s at 284.6 eV as standard and corrected if needed. The peak fitting of the individual core-levels was done using CASAXPS software with a Shirley type background.

1.7. XAFS:

Ni XAFS measurements of Ni-edge of Ni/SBA-15, Ni₇In₃/SBA-15 and Ni₃In/SBA-15 were carried out in fluorescence mode at PETRA III, P65 beamline of DESY, Germany. Pellets for the measurements were made by homogenously mixing the sample with an inert cellulose matrix to have an X-ray absorption edge jump close to one. Standard data analysis procedure was used to extract the extended X-ray absorption fine structure (EXAFS) signal from the measured absorption spectra. Background subtraction, normalization, and alignment of the XAFS data were performed by ATHENA software.

1.8. Operando DRIFTS:

The operando DRIFTS experimental were carried out using an Agilent Carey 680 FTIR Spectrometer equipped with a Harrick DRIFTS cell. The spectra were recorded at 4 cm⁻¹

resolution and each spectrum was averaged 64 times. Each sample was pre-treated at 473 K using 99.999% argon (Ar, BOC gas Ltd.) at a gas flow rate of 50 ml min⁻¹ for 1h in order to remove adsorbed water and other gas molecules. Then the temperature of the sample was increased to 723 K and gas switched to 20%H₂/Ar at 50 ml min⁻¹ for 2h reduction. After that, the temperature of the sample was annealed to 303 K under Ar flow. The spectrum of the annealed sample at 303 K was used as the background reference for the following reaction. To probe the reaction, 25%CO₂/75%H₂ gas mixture at 1 bar and a total flow rate of 50 ml min⁻¹ was first introduced to the DRIFTS cell, and then temperature was ramped from 303 to 573 K (ca. 15 K min⁻¹) to determine the relationship between temperature and the reaction intermedia. Then the reaction was maintained at 573 K for 1h to determine the surface intermedia evolution.

1.9. Computational Details:

Our first-principles calculations are based on density functional theory (DFT) as implemented in the Quantum ESPRESSO code⁸ employing plane-wave basis and ultra-soft pseudopotentials⁹ to represent the interaction between ionic cores and valence electrons. We adopt the exchange-correlation energy functional of Perdew-Burke-Ernzerhof (PBE)¹⁰ obtained within a generalized gradient approximation (GGA). We smear the discontinuity in occupation numbers of electronic states with Fermi-Dirac distribution having a smearing width ($k_B T$) of 0.04 eV. An energy cutoff of 50 Ry is used to truncate the plane-wave basis used in representation of Kohn-Sham wave functions, and of 400 Ry to represent the charge density. Optimized structures were determined through minimization of energy until the Hellmann-Feynman force on each atom is smaller than 0.03 eV/Å in magnitude. We use a supercell (2x2) to model the (111) surface of Ni₃In (Ni₄₈In₁₆) introducing a vacuum layer of 15 Å thickness parallel to the slab separating its adjacent periodic images. To this end, we modelled 2x2 in-plane supercell of its (111) surface (Ni₄₈In₁₆). Each supercell contains a slab

of 4 atomic planes of which, the bottom 2 atomic planes were kept fixed and the top 2 were allowed to relax. We sampled Brillouin-zone integrations on uniform grid of 6x6x1 k-points in the Brillouin zone of (111) surface of Ni₃In. The projected density of states of each structure was obtained from calculations on a denser, 15x15x1, k-point mesh. Calculated lattice constants of bulk Ni₃In ($a_{\text{Ni}_3\text{In}} = 3.74 \text{ \AA}$) are within the typical GGA errors with respect to their observed values ($a_{\text{Ni}_3\text{In}} = 3.73 \text{ \AA}$). Relative energies of the intermediate steps were plotted taking pristine Ni₃In (111) surface + CO₂ + 3H₂ as the reference. We simulated adsorption of various intermediates occurring during the CO₂ reduction reaction (CO₂RR) and calculated their adsorption energies (see methods for details)

$$\Delta E_{\text{ads}} = E_{\text{adsorbate} + \text{Ni}_3\text{In}} - (E_{\text{Ni}_3\text{In}} + E_{\text{adsorbate}})$$

where, $E_{\text{adsorbate} + \text{Ni}_3\text{In}}$, $E_{\text{Ni}_3\text{In}}$ and $E_{\text{adsorbate}}$ are the energies of adsorbate locally stabilized on Ni₃In (111) surface, bare Ni₃In (111) surface and the adsorbate molecule, respectively. The transition states (TSs) were obtained using the nudged elastic band (NEB)¹¹ method. Five images were used in all the NEB calculations in this paper. All transition states were fully relaxed until the Hellmann–Feynman forces acting on the atoms were within 0.05 eV Å.

2. Data Calculations

2.1. Weight Hour Space Velocity (WHSV):

WHSV is defined as the mass of reactant per unit time passed per mass of catalyst charged in a reactor. Here we used two flow rates 40 NLPH (1CO₂:3H₂) and 50 NLPH (1CO₂:4H₂).

40 NLPH:

CO₂ flow = 10 NLPH (19.8 grams per hour)

H₂ flow = 30 NLPH (2.67 grams per hour)

N₂ flow (internal standard for GC analysis) = 0.8 NLPH (1 grams per hour)

Mass of catalyst charged = 5 g

$$\text{WHSV} = (19.8 + 2.67 + 1)/5 = 4.69 \text{ h}^{-1} = \sim 4.7 \text{ h}^{-1}$$

50 NLPH:

CO₂ flow = 10 NLPH (19.8 grams per hour)

H₂ flow = 40 NLPH (3.56 grams per hour)

N₂ flow (internal standard for GC analysis) = 1 NLPH (1.25 grams per hour)

Mass of catalyst charged = 5 g

$WHSV = (19.8 + 3.56 + 1.25)/5 = 4.922 \text{ h}^{-1} = \sim 4.9 \text{ h}^{-1}$

2.2. Response factor of GC (RF):

Response factor for a component 'i' of a detector is the ratio of peak area of component 'i' to calibration concentration (eqn. 1). The unknown concentration of component 'i' during online gas analysis is determined multiplying response factor of component with peak area of the component obtained during online analysis. Note that calibration compositions of samples are expressed in percentage.

$$RF_i = \text{Peak Area of } i \div \text{Std. composition of } i \text{ in percentage} \quad (1)$$

$$\text{Unknown composition of } i \text{ in product gas (\%)} = RF \times \text{Peak area of } i \text{ in product} \quad (2)$$

The GC RF for TCD are given below:

RF of CO₂ = 0.001617

RF of N₂ = 0.001848

RF of CO = 0.00216

RF of CH₄ = 0.00221

2.3. Conversion and product selectivity

$$\text{CO}_2 \text{ conversion in \%} = \left(\text{CO}_2(\text{in}) - \text{CO}_2(\text{out}) \times \frac{N_2(\text{out})}{N_2(\text{in})} \right) \div \text{CO}_2(\text{in}) \quad (3)^{12}$$

$$\text{Selectivity of } i = (100n \times \text{comp of } i / N_2(\text{out})) \div \left(\frac{CO_2(\text{in})}{N_2(\text{in})} - \frac{CO_2(\text{out})}{N_2(\text{out})} \right) \quad (4)$$

$$\text{MeOH selectivity (\%)} = 100 - (\text{CO selectivity} + \text{CH}_4 \text{ selectivity}) \quad (5)$$

CO₂(in) = composition of CO₂ in feed gas

CO₂(out) = composition of CO₂ in product

N₂(in) = composition of N₂ in feed gas

N₂(out) = composition of N₂ in product

2.4 Liquid analysis

The liquid products reaction is collected by condensation after 15 hours of reaction. The condensed liquid is analyzed for methanol by auto-liquid sampler of GC with FID as a detector. The liquid analysis is done by mixing 1.5 ml of liquid product with 100 µl of isopropyl alcohol (IPA). A calibration plot of different MeOH volume % vs peak area ratio of MeOH to IPA is plotted by making different standards of MeOH-water mixture as shown in Figure below (**Figure S5**). The MeOH volume % of unknown sample is determined from peak area ratio of MeOH/IPA peak area by GC.

$$\text{MeOH selectivity by gas analysis} = [100 - (S_{\text{CO}} + S_{\text{CH}_4})] \% \quad (6)$$

Ni₇In₃/SBA-15-573K-50B-4.7 h⁻¹

Conversion = 17 %

CO selectivity = ~12.75 %

CH₄ selectivity = 0.4 %

From eqn (6), MeOH selectivity = 100 – (12.75 + 0.4) = 86.85 %

Out of 100 moles of product 86.85 moles are MeOH, 12.75 are CO and negligible 0.4 % are CH₄.



$$\text{MeOH mol \% in liquid product} = 86.85 \times \frac{100}{86.85 + 86.85 + 12.75 + 0.8}$$

Each mole of methanol and carbon monoxide gives one mole of water while each mole of methane gives 2 moles of water.

Thus, in liquid product MeOH mol % = 46.4 %

$$\text{MeOH weight \% in liqd.} = (100 \times 46.4 \times 32) \div ((46.4 \times 32) + (53.6 \times 18))$$

$$\text{MeOH weight \% in liqd.} = 60.6\%$$

From density of methanol (0.791 gml⁻¹) and water (1gml⁻¹),

MeOH vol. % in liqd. = 66.04% (expected volume % of Methanol in liquid by gas analysis)

The average peak area ratio is 6.24

$$\text{MeOH vol. \% in liqd.} = (6.24 \times 9.154) + 0.246$$

MeOH vol. % in liqd. = 57.37% (The value is lesser than expected by gas analysis, this may be due to evaporation losses of MeOH during liquid condensation)

Similarly, liquid analysis is presented in table below

MeOH (PA)	IPA (PA)	MeOH/IPA
2995	464	6.45
2890	462	6.25
2895	464	6.24

Refer Table S2 for liquid analysis

3. Electronic structure of intermediates along competing pathways of CO₂ on Ni₃In (111)

To shed light on the nature of bonding between intermediates and the catalyst, we examine the projected density of states (PDOS) of the first intermediates occurring along the formate and *cis*-COOH pathways of CO₂ reduction on the (111) surface of Ni₃In: *bi*-HCOO*Ni₃In and *trans*-COOH*Ni₃In, respectively. The PDOS of *bi*-HCOO*Ni₃In and *trans*-COOH*Ni₃In reveal the highest occupied molecular orbitals (HOMO) of the adsorbates lie close to the bottom of the 3d-bands of Ni. HOMO of **bi*-HCOO exhibits a sharp peak close to -3.5 eV, (similar to HOMO of *CO₂) accompanied by another smaller peak at a slightly higher energy. The degeneracy in the HOMO peaks is because of charge transfer from the surface to the adsorbate (see Fig. S14), which is also evident from the Lowdin charges that show a reduction the occupancy of Ni-3d and In-5s orbitals and an increased occupancy of O-2p orbitals of both the O-atoms of HCOO (Table S4). Also, HOMO of *bi*-HCOO splits and broadens because of its covalent interaction with the In-5p and Ni-4p orbitals of the catalyst, which are in resonance. HOMO of **trans*-COOH lies deeper in energy and resonates with Ni-3d, Ni-4p and In-5p orbitals of the surface. Lowdin charge analysis shows a charge transfer from the Ni₃In surface to the adsorbate. We find a decrease in the number of electrons in Ni-3d states due to transfer to C-2s and C-2p orbitals (Table S4).

4. Tables

Table S1. Catalytic performances of different catalyst with respect to the reaction condition.

Catalyst	Reaction Condition	Conversion (%)	Selectivity towards MeOH (%)	Selectivity Towards CO (%)	Selectivity Towards CH ₄ (%)
SBA-15	573K-20B-4.7/h	<0.001	-	100	-
	573K-20B-4.7/h	<0.001	-	100	-
Ni/SBA-15	573K-40B-4.7/h	60	-	<0.05	>99.5
	573K-40B-4.9/h	80	-	<0.05	>99.5
	573K-20B-4.7/h	50	-	<0.05	>99.5
	573K-20B-4.9/h	68	-	<0.05	>99.5
	573K-20B-4.7/h	17.5	87-88	12-13	<1
Ni ₃ In/SBA-15	573K-40B-4.7/h	17	79	20	0.5
	573K-40B-4.9/h	14.8	63	36	0.55
	523K-40B-4.7/h	4.75	73	27	-
	523K-40B-4.9/h	6	83	17.8	-
	573K-20B-4.7/h	16-16.5	75	23.8	0.04
	573K-20B-4.9/h	13	67	32	0.08
	523K-20B-4.7/h	4.5	83	17	-
	523K-20B-4.9/h	4	85	14	-
	573K-5B-4.7/h	<1	-	100	-
	573K-10B-4.7/h	1-2	1	99 -100	-
	573K-15B-4.7/h	15.8	75	13-14	2
NiO-In ₂ O ₃ /SBA-15	573K-50B-4.7/h	9	75	24	<1
	573K-40B-4.7/h	11	77	22	< 1
	573K-20B-4.7/h	10.5	85	14.5	0.5

Table S2. Methanol selectivity by liquid analysis.

Catalyst	Reaction condition	MeOH vol.% by gas analysis	Ratio of MeOH/IPA	MeOH vol. % by liquid analysis
Ni ₇ In ₃ /SBA-15	573K-50B-4.7/h	66.04	6.24	57.47
	573K-40B-4.7/h	63.96	5.76	53.03
	573K-20B-4.7/h	63.18	5.98	54.98
	573K-40B-4.9/h	58.58	5.55	51.05
	573K-20B-4.9/h	55.04	5.16	47.46
	523K-40B-4.7/h	61.76	4.66	42.81
	523K-20B-4.7/h	65.10	6.03	55.45
	523K-40B-4.9/h	65.1	6.02	55.36
	523K-20B-4.9/h	65.1	5.19	47.77
	573K-50B-4.7/h	62.65	5.77	53.11
NiO-In ₂ O ₃ /SBA-15	573K-40B-4.7/h	63.15	6.33	58.17
	573K-20B-4.7/h	65.53	6.21	57.1

Table S3. Summary of Ni 2p XPS spectrum of Ni₇In₃/SBA-15 and Ni₃In/SBA-15

Chemical State	Ni ₇ In ₃ /SBA-15		Ni ₃ In/SBA-15	
	Binding Energy (eV)	Peak Area	Binding Energy (eV)	Peak area
Ni ²⁺ 2p _{3/2}	855.69	23566	856.462	10000
Ni ²⁺ 2p _{1/2}	873.055	6554	874.379	5932.2
Ni ⁰ 2p _{3/2}	851.627	5764.3	852.11	4734.8
Ni ⁰ 2p _{1/2}	869.318	2566.8	870.493	3483.2

Table S4. Calculated Lowdin charges of Ni, In, C and O atoms for (a) pristine (111) surface of Ni₃In, (b) isolated CO₂ molecule, and (c) CO₂, (d) *bi*-HCOO and (e) *trans*-COOH adsorbed on the (111) surface of Ni₃In, respectively.

Sample	Atom	Number of Valence electrons			Total number of valence electrons	Valence configuration in pseudopotential
		s	p	d		
(a) Ni ₃ In	Ni	0.42	0.99	8.8	10.21	4s ² 3d ⁸ (10)
	In	0.8	1.46	9.94	12.2	5s ² 4d ¹⁰ 5p ¹ (13)
(b) CO ₂ isolated	C	0.74	2.46	0	3.2	2s ² 2p ² (4)
	O	1.66	4.61	0	6.27	2s ² 2p ⁴ (6)
(c) Ni ₃ In (CO ₂ adsorbed)	Ni _C	0.42	1.09	8.76	10.27	4s ² 3d ⁸ (10)
	Ni _O	0.4	1.03	8.72	10.15	4s ² 3d ⁸ (10)
	C	0.88	2.61	0	3.49	2s ² 2p ² (4)
	O	1.63	4.64	0	6.27	2s ² 2p ⁴ (6)
	In	0.79	1.44	9.94	12.17	5s ² 4d ¹⁰ 5p ¹ (13)
(d) Ni ₃ In (<i>bi</i> -HCOO adsorbed)	Ni _{O1}	0.4	1.06	8.72	10.18	4s ² 3d ⁸ (10)
	In _{O2}	0.73	1.43	9.95	12.11	5s ² 4d ¹⁰ 5p ¹ (13)
	O1	1.66	4.73	0	6.39	2s ² 2p ⁴ (6)
	O2	1.61	4.71	0	6.32	2s ² 2p ⁴ (6)
(e) Ni ₃ In (<i>trans</i> -COOH adsorbed)	Ni _C	0.4	1.19	8.72	10.34	4s ² 3d ⁸ (10)
	Ni _O	0.39	1.02	8.74	10.15	4s ² 3d ⁸ (10)
	C	0.97	2.6	0	3.57	2s ² 2p ² (4)
	O	1.63	4.63	0	6.26	2s ² 2p ⁴ (6)
	In	0.79	1.44	9.95	12.17	5s ² 4d ¹⁰ 5p ¹ (13)

Table S5. Important examples of intermetallic and bimetallic catalyst for CO₂ hydrogenation to methanol.

Catalyst	Synthesize route	Reaction Condition	Conversion (%)	Selectivity (%)	Ref
CuNi ₂ /CeO ₂ (bimetallic)	Impregnation	533 K, 30 bar and 6000 h ⁻¹ (GHSV).	17.8.	78	¹³
PdIn IMC NP	Thermal decomposition of metal acetate in squalane	483 K and 50 bar.	3	80	¹⁴
Pd ₂ Ga colloidal NP	Colloidal synthesize in CSTR 300 ml Parr reactor.	483 K and 50 bar.	3	75	¹⁵
In:Pd(2:1)/SiO ₂	Incipient wetness impregnation	573 K and 50 bar	5.1 μmol/g	61	¹⁶
Cu ₁₁ In ₉ /In ₂ O ₃	CuO-In ₂ O ₃ heterostructure reduced at 623 K	553 K and 30 bar	11.4	80.5	¹⁷
Ni ₅ Ga ₃ /SiO ₂	Incipient wetness impregnation	493 K, atm. Pressure and 6000 h ⁻¹ (GHSV).		~0.25 mol/hr	¹⁸

5. Figures

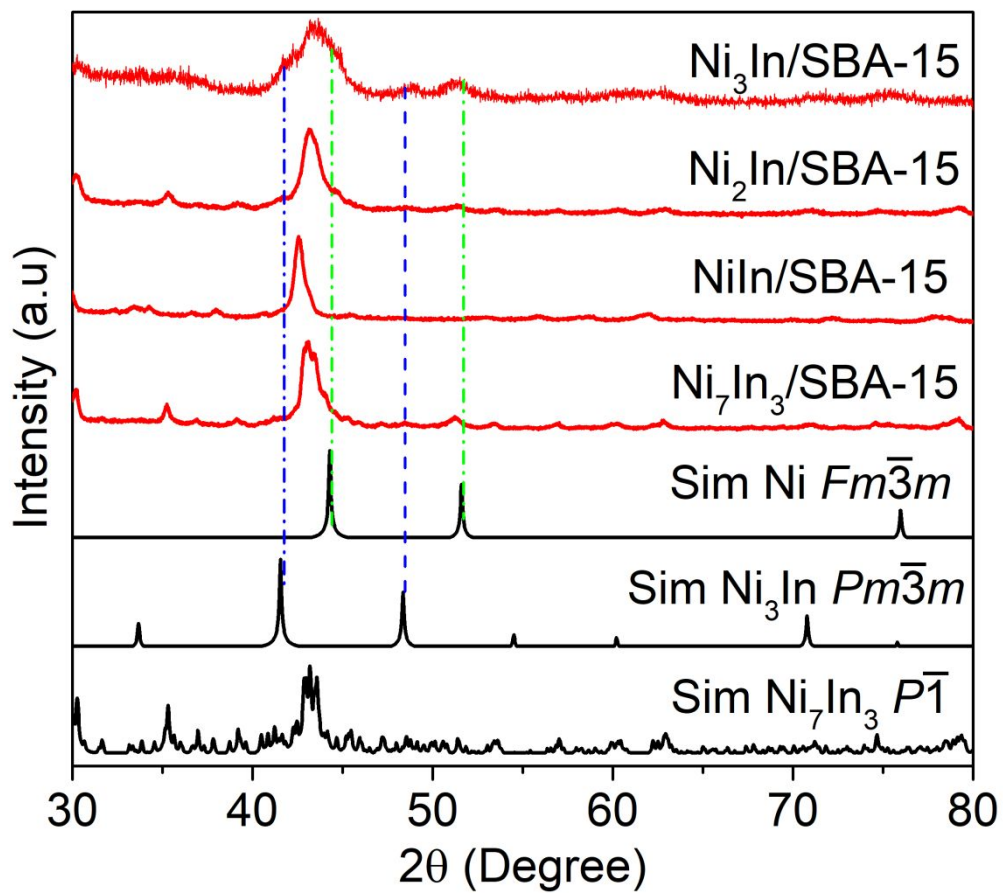


Figure S1. Powder XRD pattern of Ni₃In/SBA-15, Ni₂In/SBA-15, NiIn/SBA-15, Ni₇In₃/SBA-15, simulated Ni $Fm\bar{3}m$, simulated Ni₃In $Pm\bar{3}m$ and simulated Ni₇In₃ $P\bar{1}$.

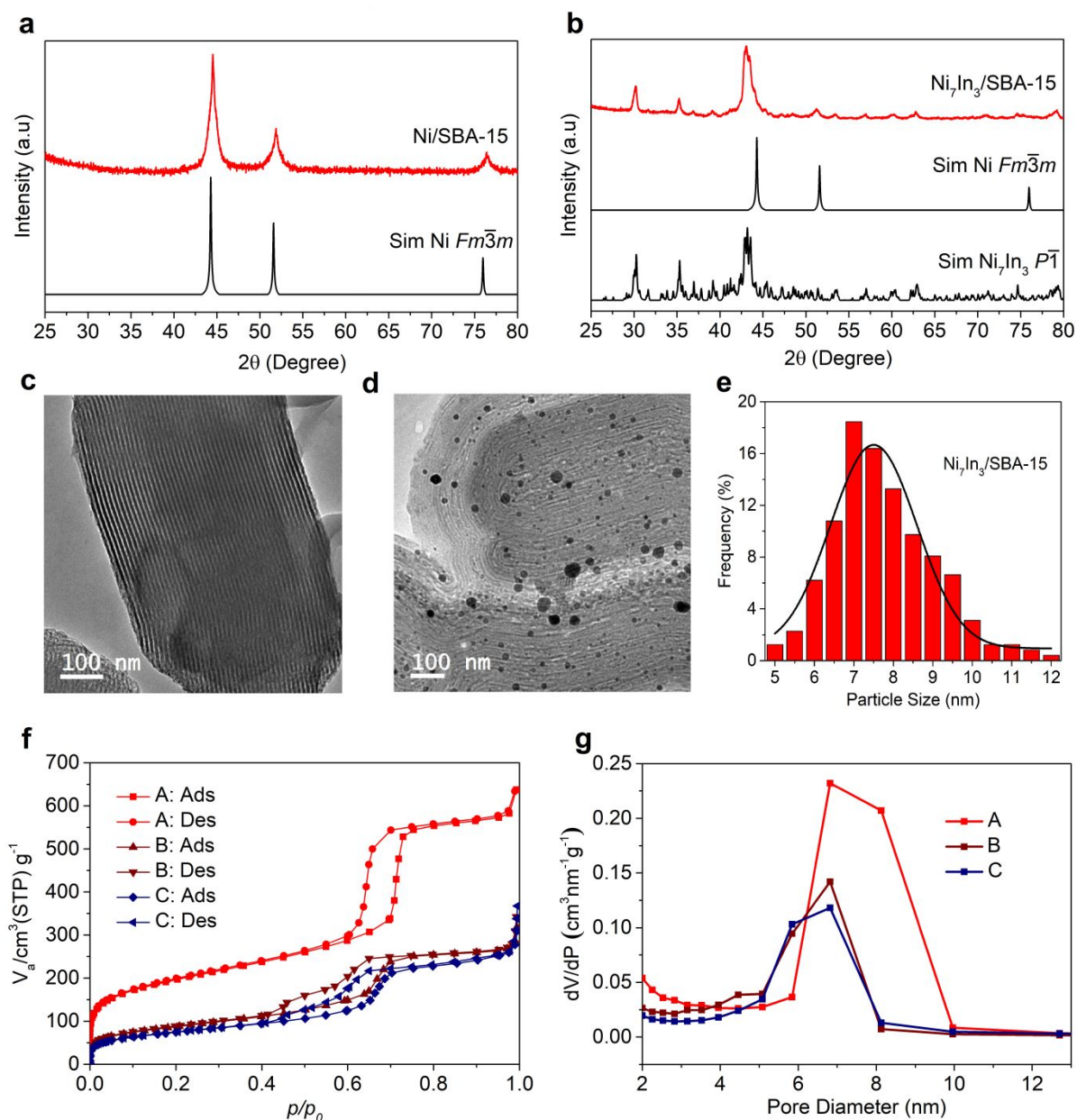


Figure S2. Powder XRD pattern comparison between experimental Ni/SBA-15 and simulated Ni (SG: $Fm\bar{3}m$). b, Powder XRD pattern comparison between experimental Ni₇In₃/SBA-15, simulated pattern of Ni (SG: $Fm\bar{3}m$) and simulated pattern of Ni₇In₃ (SG: $P\bar{1}$). c, TEM image of SBA-15. d, TEM image of Ni₇In₃/SBA-15. e, Particle size distribution of Ni₇In₃ on SBA-15. f, N₂ adsorption-desorption isotherm of A: SBA-15, B: Ni/SBA-15 and C: Ni₇In₃/SBA-15 at 77 K. g, corresponding pore size distribution by BJH method.

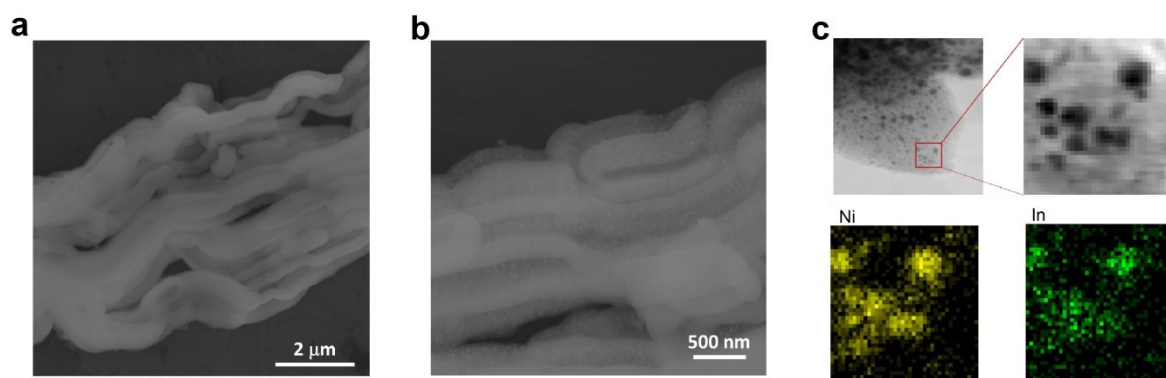


Figure S3. Material Characterization. **a**, SEM image of SBA-15. **b**, SEM image of Ni₇In₃/SBA-15. **c**, STEM and elemental color mapping of nanoparticles,

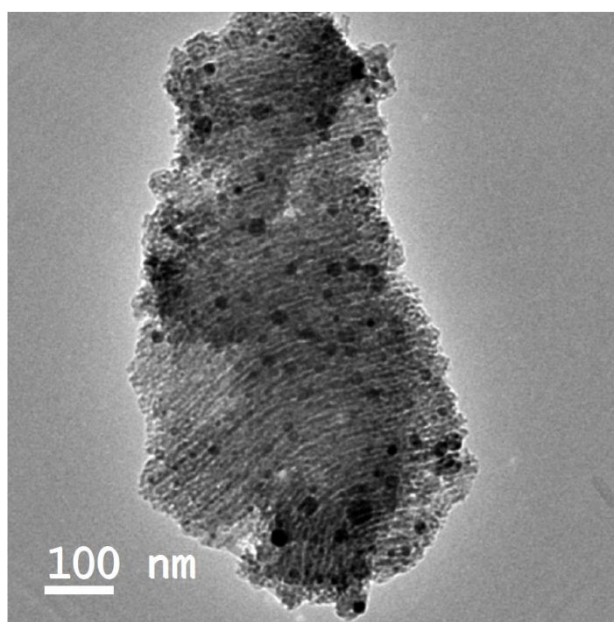


Figure S4. TEM image of Ni/SBA-15.

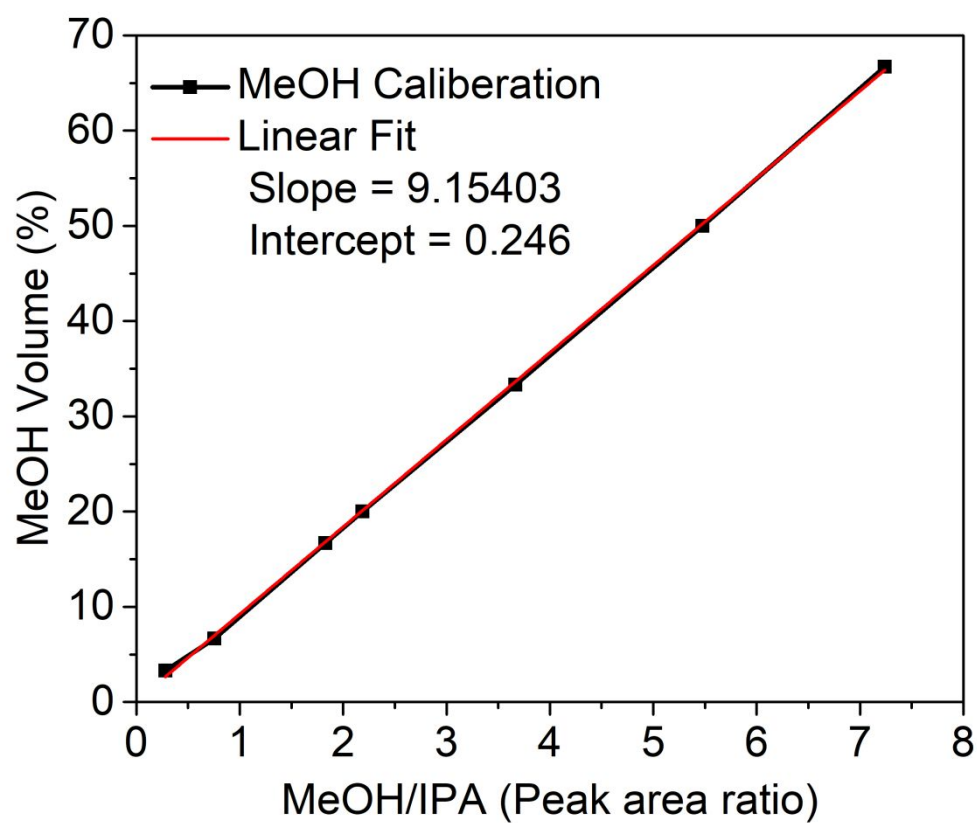


Figure S5. Calibration curve for liquid analysis

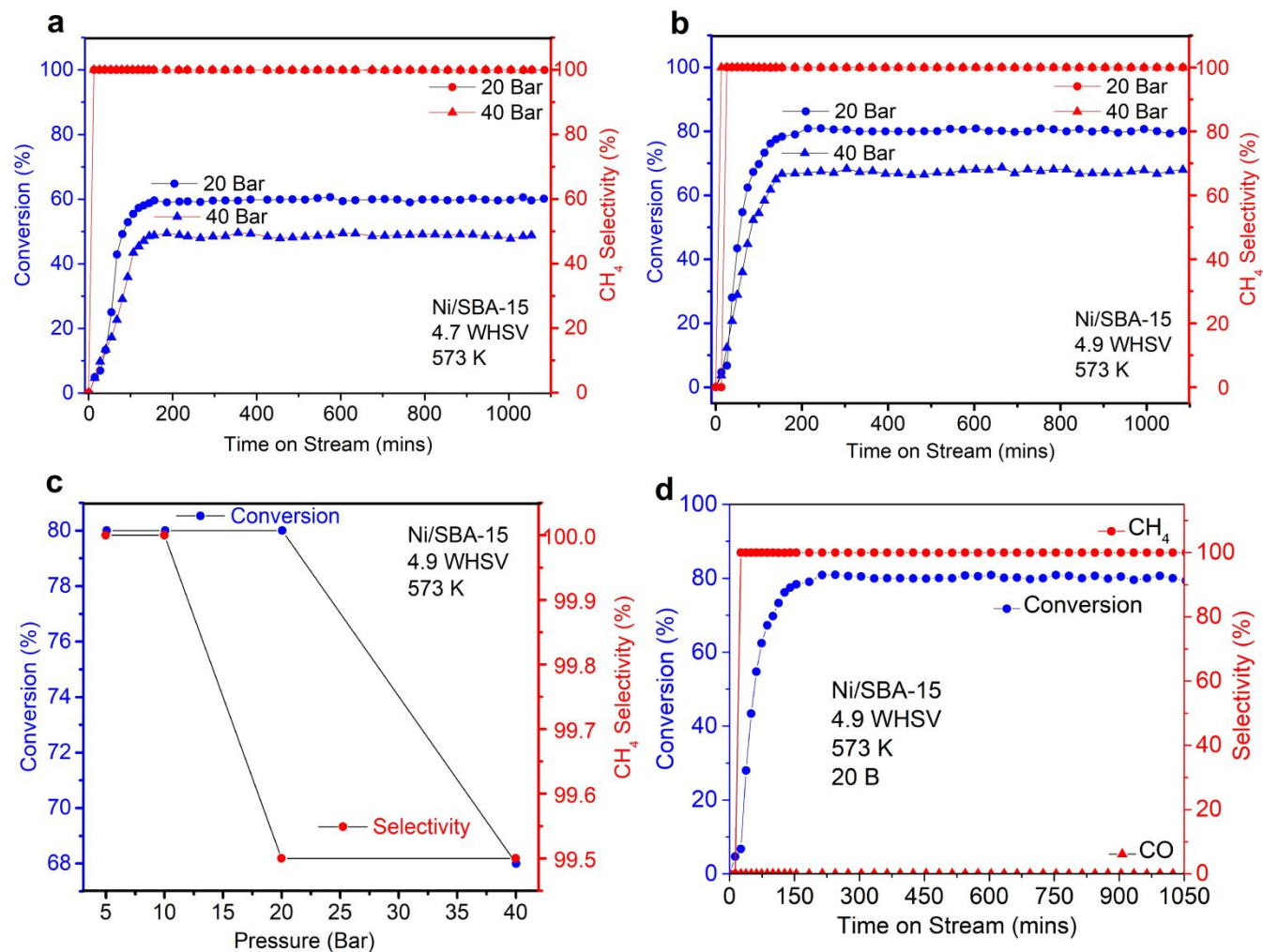


Figure S6. Catalytic performance of Ni/SBA-15. **a**, CO₂ conversion and methane selectivity at reaction condition of 20 bar and 40 bar pressure with WHSV 4.7 h⁻¹ (CO₂/H₂=1:3) and at 573 K temperature. **b**, CO₂ conversion and methane selectivity at reaction condition of 20 bar and 40 bar with 4.9 h⁻¹ (CO₂/H₂=1:4) and 573 K. **c**, CO₂ conversion and methane selectivity at different pressures (5-40 bar) with 4.9 h⁻¹ and 573 K. **d**, CO₂ conversion and selectivity for 15 hours of time on stream at reaction condition of 4.9 h⁻¹, 20 bar and 573K

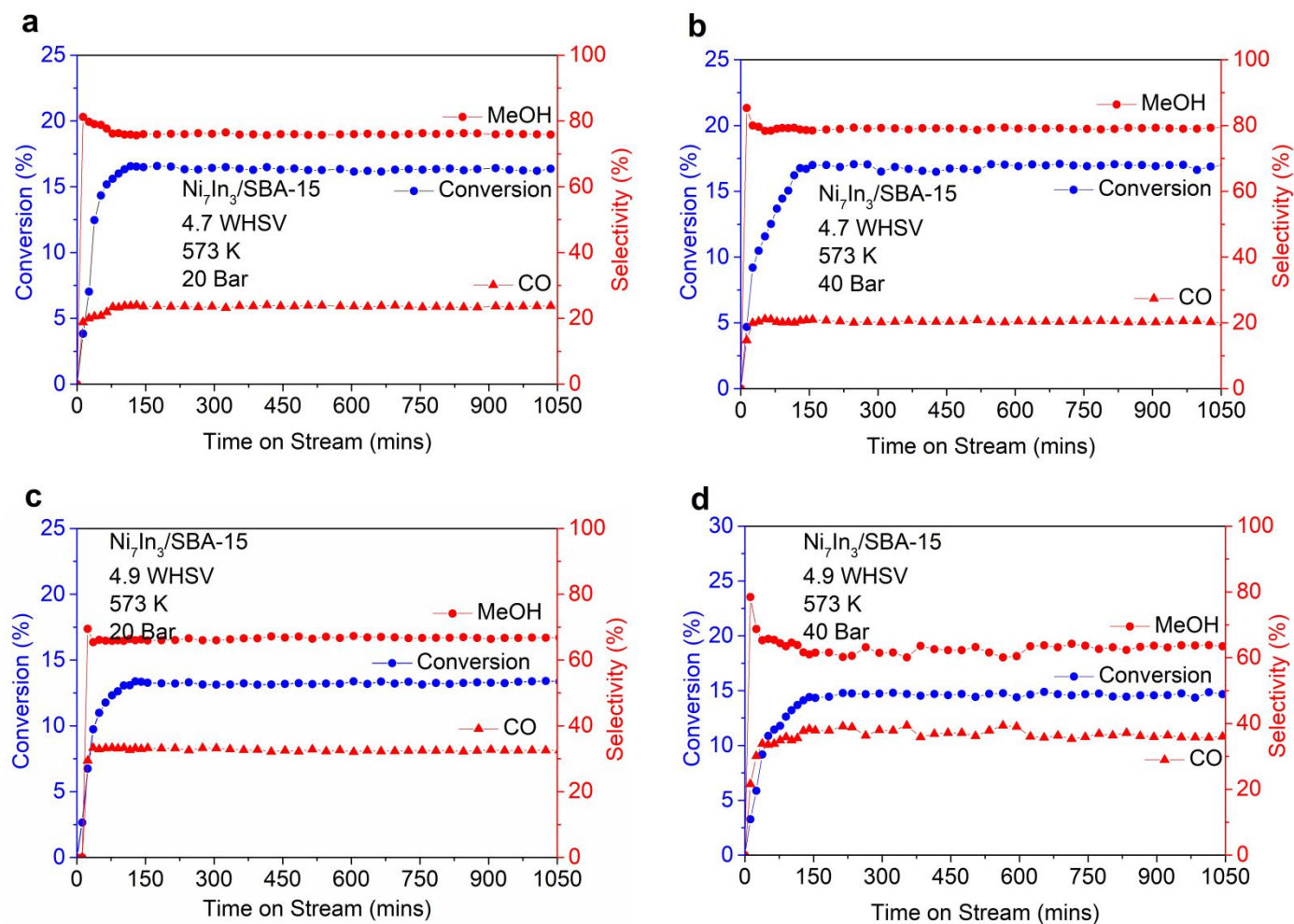


Figure S7. Catalytic test on $\text{Ni}_7\text{In}_3/\text{SBA-15}$ at 573 K. a, CO_2 conversion and selectivity for 15 hours of time on stream at reaction condition of 4.7 h^{-1} (1:3) and 20 bar. **b,** CO_2 conversion and selectivity for 15 hours of time on stream at reaction condition of 4.7 h^{-1} (1:3) and 40 bar. **c,** CO_2 conversion and selectivity for 15 hours of time on stream at reaction condition of 4.9 h^{-1} (1:4), and 20 bar. **d,** CO_2 conversion and selectivity for 15 hours of time on stream at reaction condition of 4.9 h^{-1} (1:4) and 40 bar.

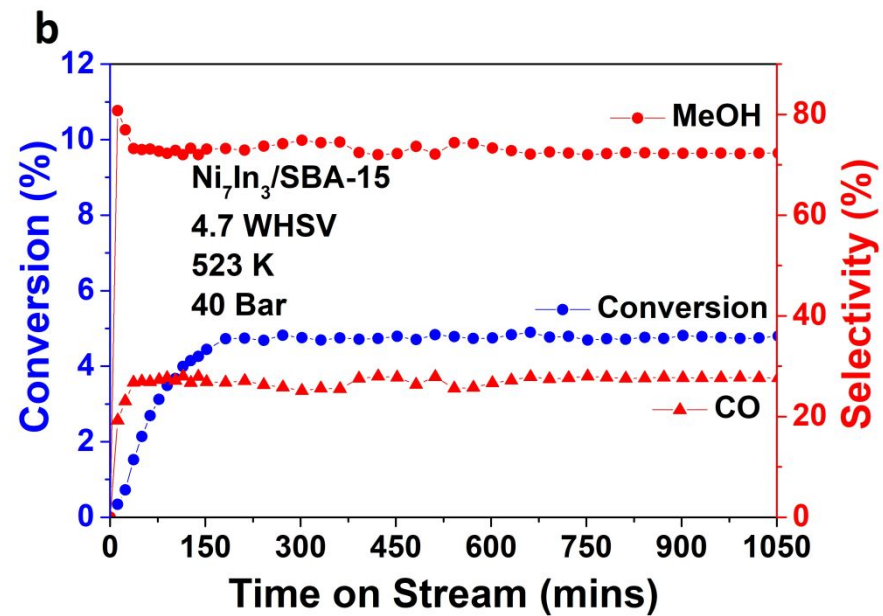
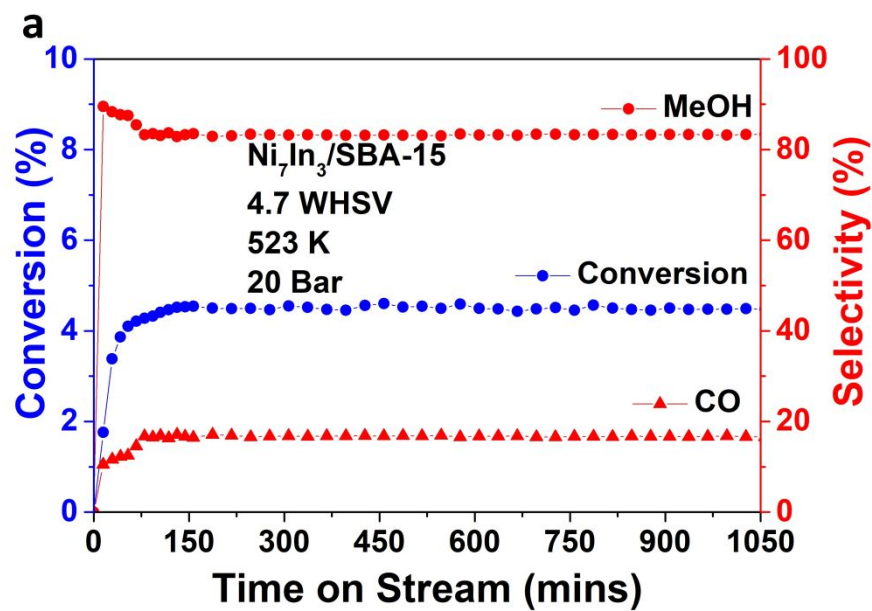


Figure S8. Catalytic test on $\text{Ni}_7\text{In}_3/\text{SBA-15}$ at 523 K. **a**, CO_2 conversion and selectivity for 15 hours of time on stream at reaction condition of 4.7 h^{-1} (1:3) and 20 bar. **b**, CO_2 conversion and selectivity for 15 hours of time on stream at reaction condition of 4.7 h^{-1} (1:3) and 40 bar.

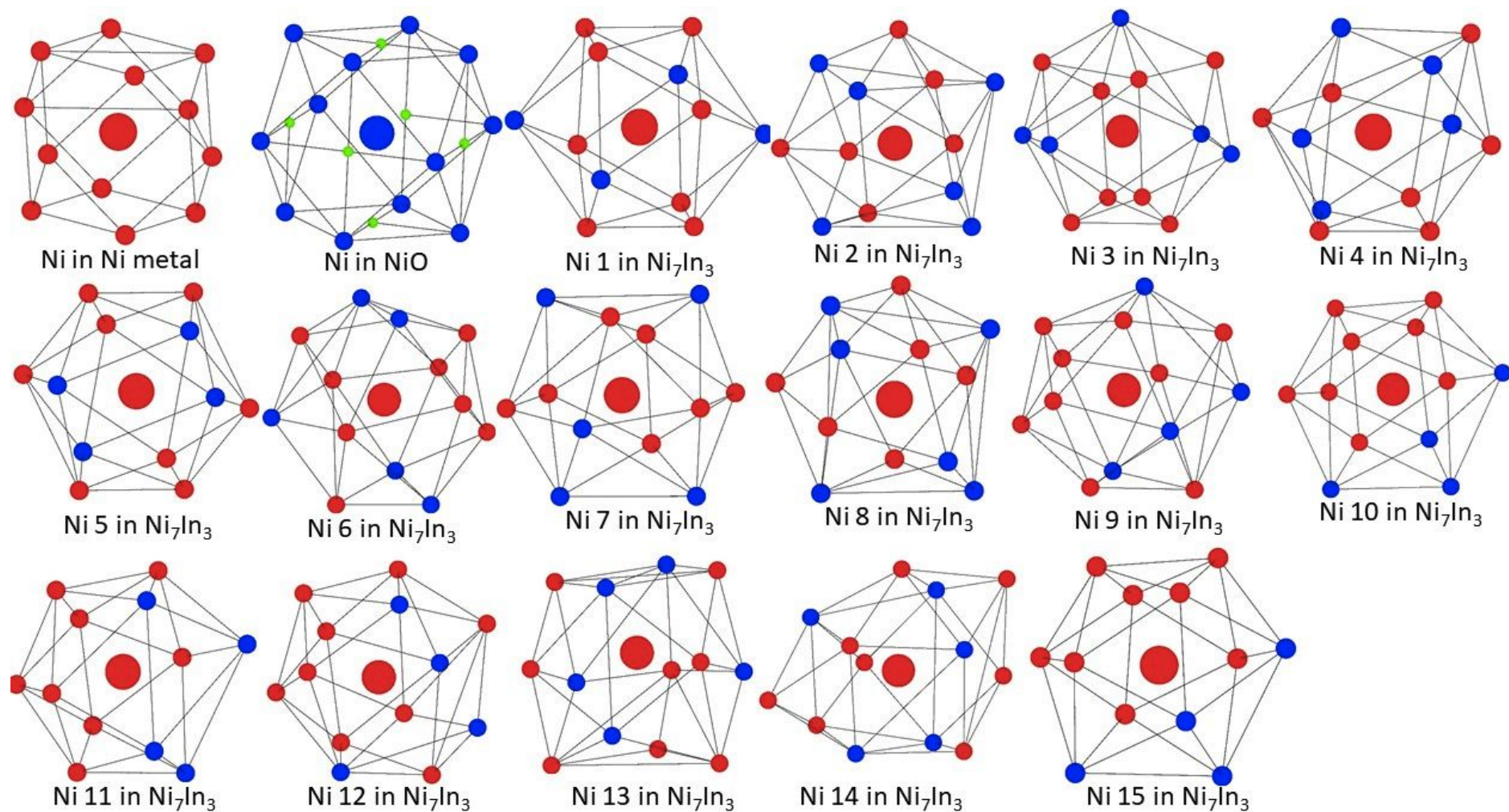


Figure S9. Coordination environment of Ni in Ni metal, NiO, Ni_7In_3 and Ni_3In .

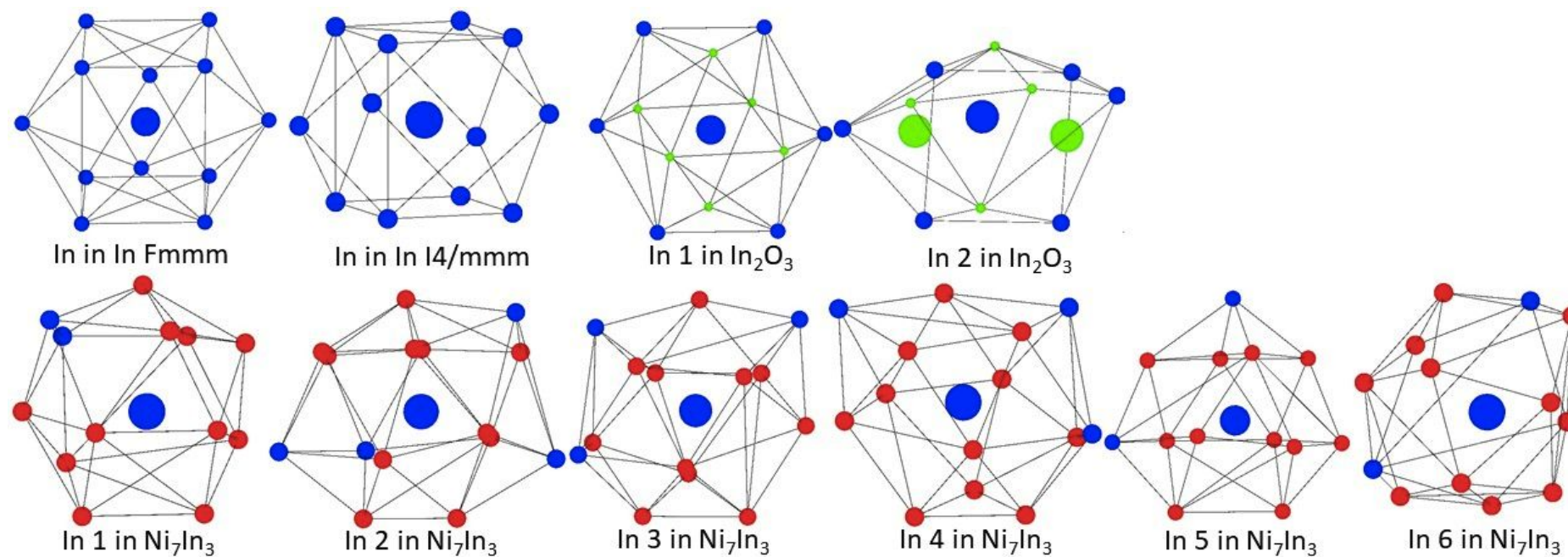


Figure S10. Coordination environment of In in In metal, Ni_7In_3 , Ni_3In and In_2O_3

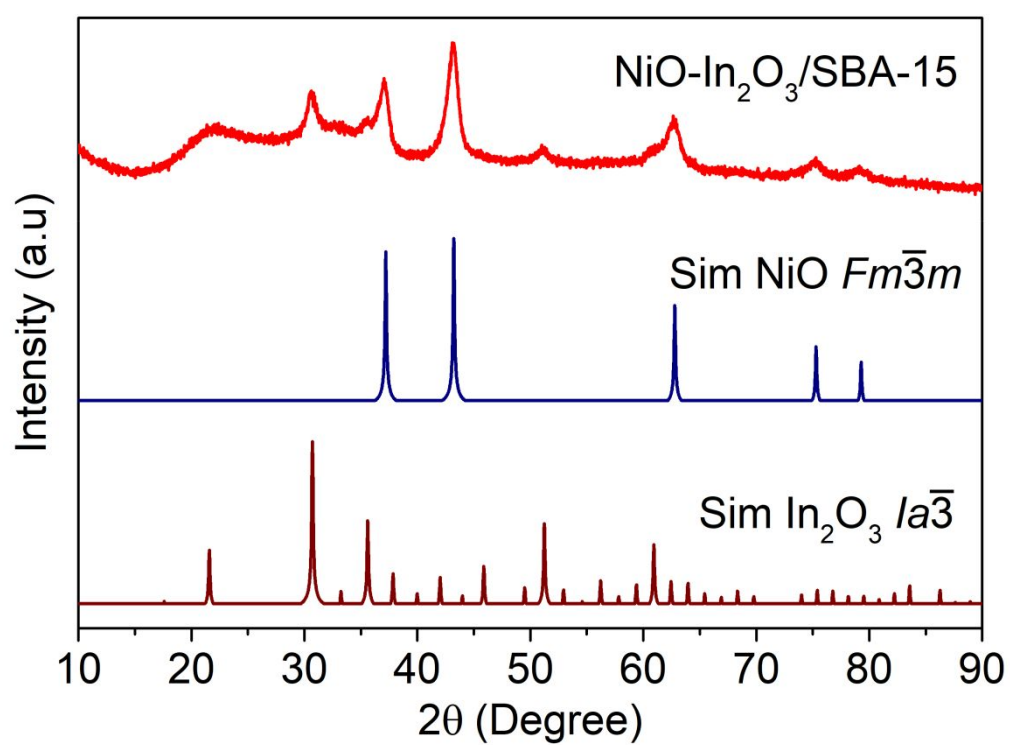


Figure S11. Powder XRD pattern of $\text{NiO-In}_2\text{O}_3/\text{SBA-15}$, simulated $\text{NiO } Fm\bar{3}m$ and simulated $\text{In}_2\text{O}_3 Ia\bar{3}$.

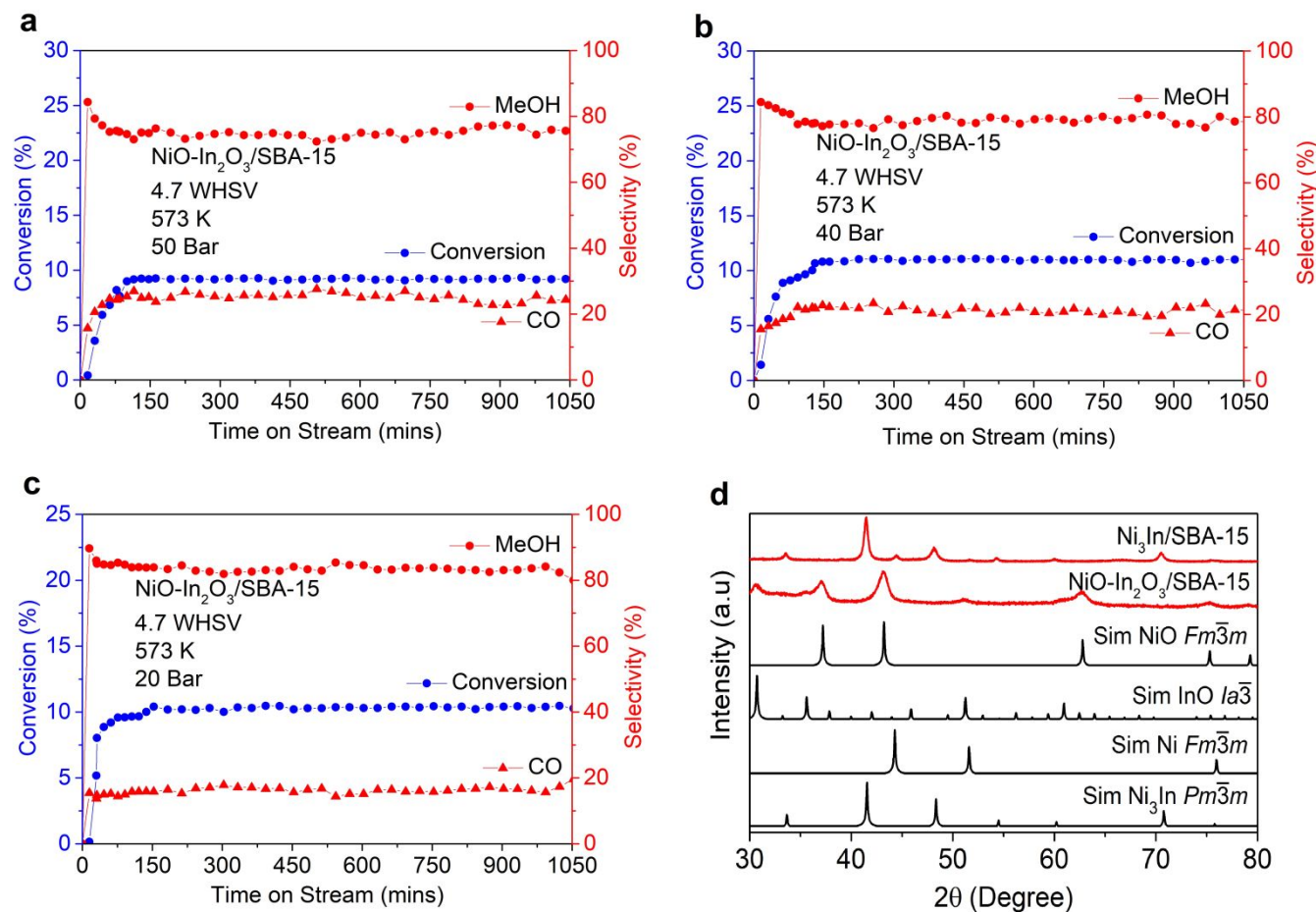


Figure S12. Catalytic performance of $\text{NiO-In}_2\text{O}_3/\text{SBA-15}$ at 573 K. a, CO₂ conversion and selectivity for 15 hours of time on stream at reaction condition of 4.7 h⁻¹ (1:3) and 50 bar. **b,** CO₂ conversion and selectivity for 15 hours of time on stream at reaction condition of 4.7 h⁻¹ (1:3) and 40 bar. **c,** CO₂ conversion and selectivity for 15 hours of time on stream at reaction condition of 4.7 h⁻¹ (1:3) and 20 bar. **d,** Comparison of the powder XRD patterns of experimental $\text{Ni}_3\text{In}/\text{SBA-15}$ and $\text{NiO-In}_2\text{O}_3/\text{SBA-15}$ with the simulated patterns of NiO (SG: $Fm\bar{3}m$), In_2O_3 (SG: $Ia\bar{3}$), (SG: $\text{Ni } Fm\bar{3}m$) and Ni_3In (SG: $Pm\bar{3}m$).

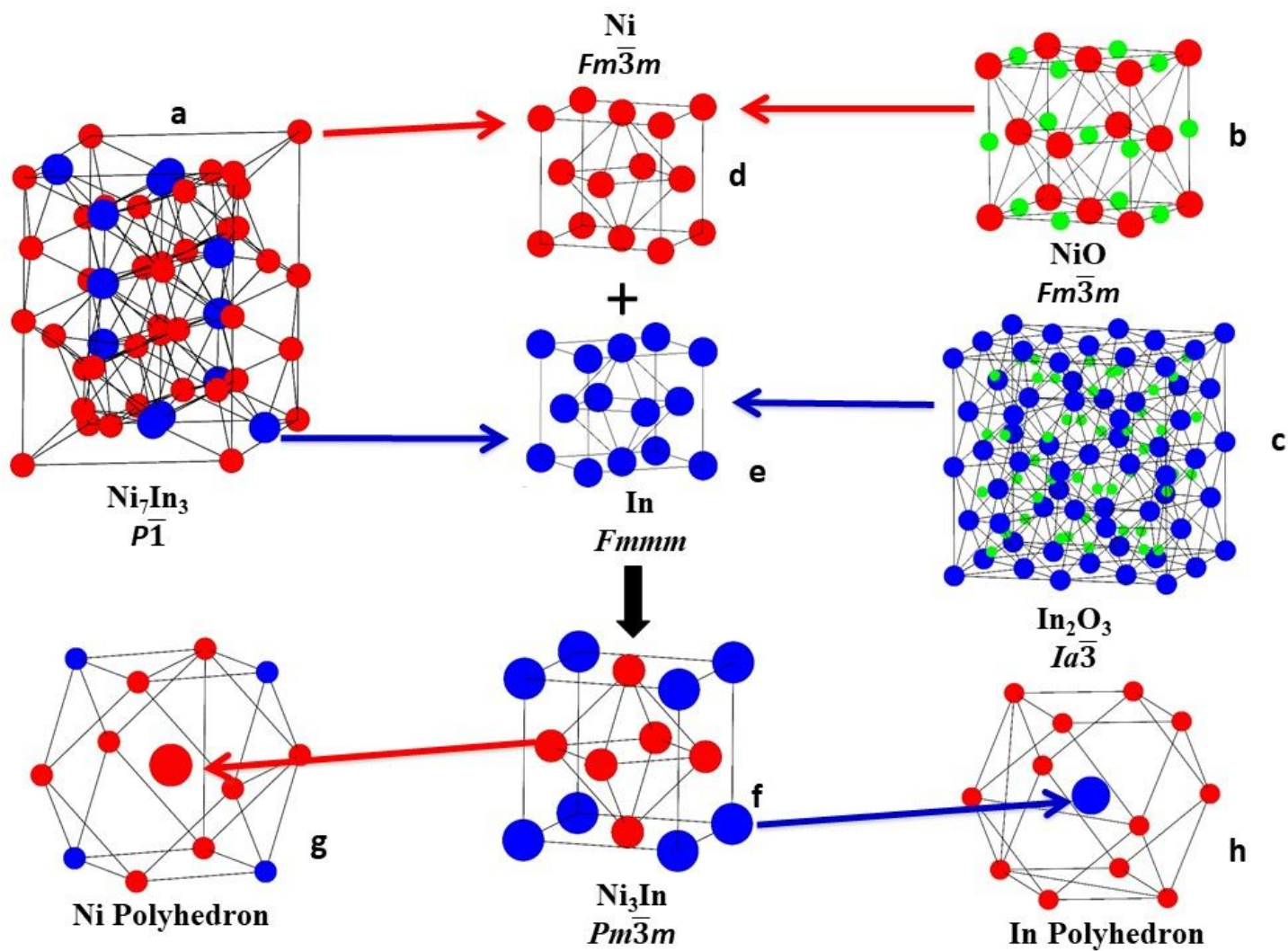


Figure S13. Operando structural phases transformation of different starting materials Ni_7In_3 /SBA-15 (a), and $\text{NiO-In}_2\text{O}_3$ /SBA-15 (b and c) to Ni_3In /SBA-15 (f) through the intermediates Ni (d) and In (e) metals under 573 K and above 20 bar pressure. The coordination environment of Ni (g) and In (h) in Ni_3In structure.

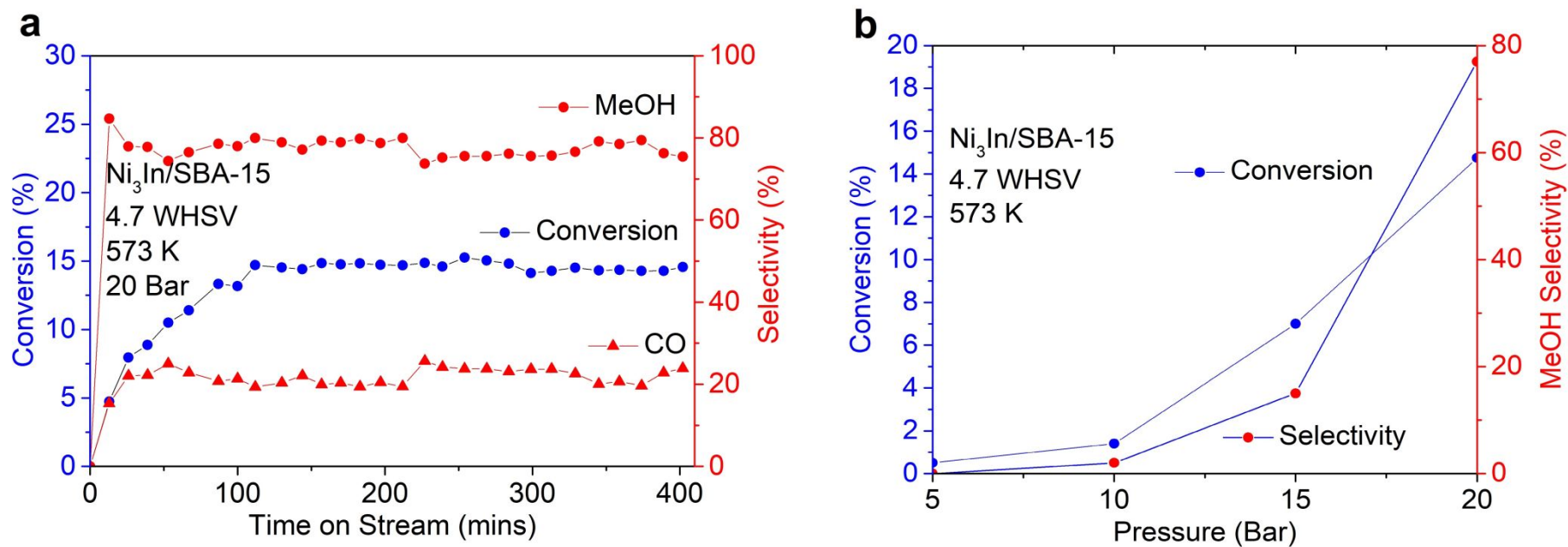


Figure S14. Catalytic performance of $\text{Ni}_3\text{In/SBA-15}$. **a**, CO₂ conversion and selectivity for 6 hours of time on stream at reaction condition of 4.7 h⁻¹ (1:3) and 20 bar. **b**, CO₂ conversion and methanol selectivity at different pressures (5-20 bar) with 4.7 h⁻¹ and 573 K.

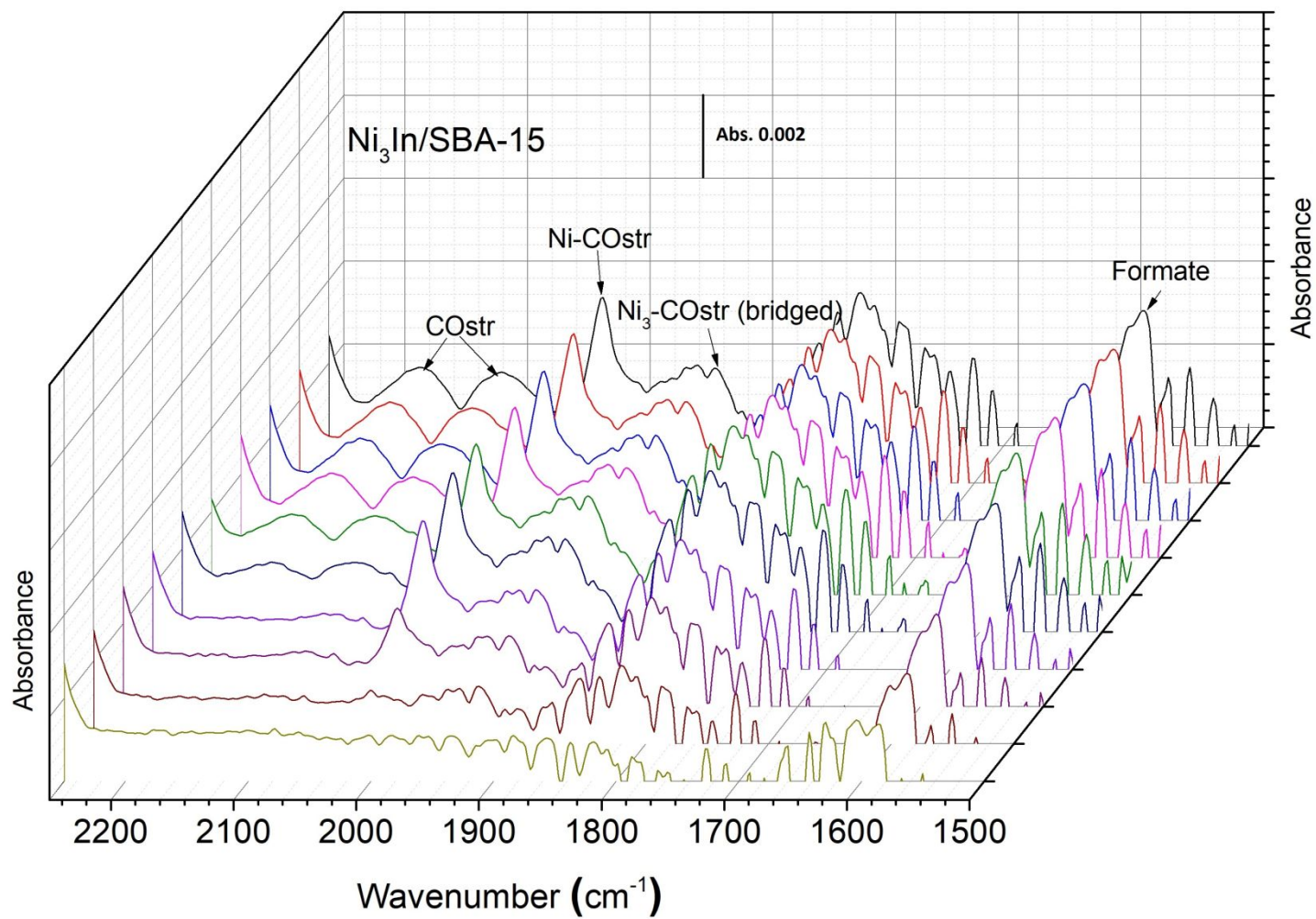


Figure S15. Successive DRIFTS spectra of formate and CO stretching regions over $\text{Ni}_3\text{In/SBA-15}$ plotted against time over $\text{Ni}_3\text{In/SBA-15}$.

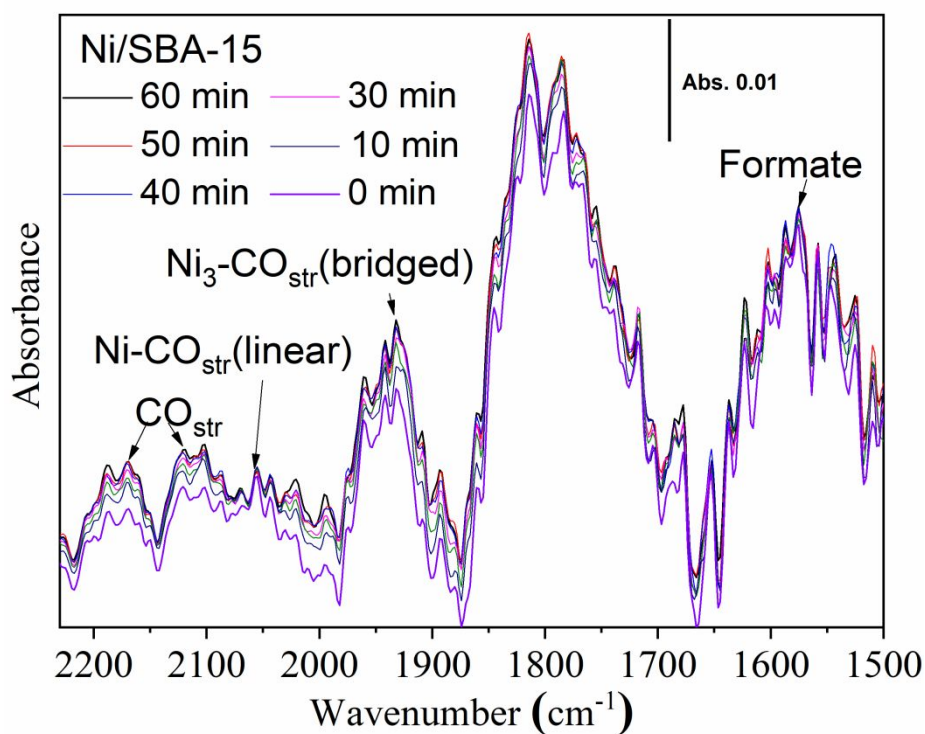


Figure S16. Successive DRIFTS spectra of formate and CO stretching regions over Ni/SBA-15 for an hour on stream.

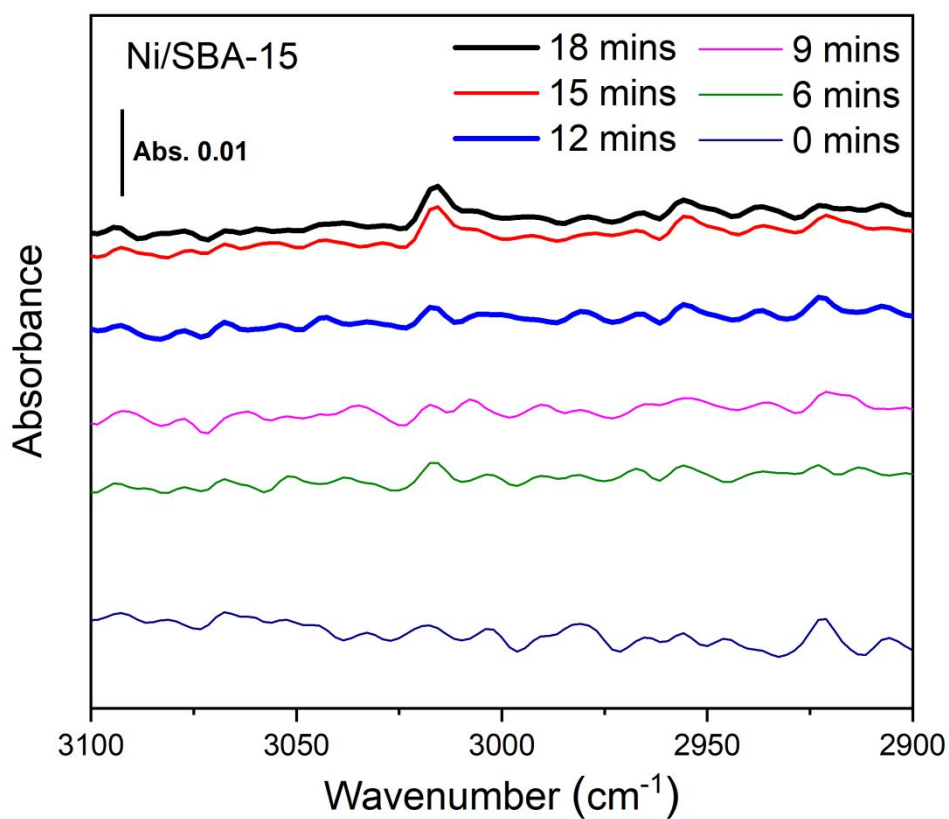


Figure S17. Successive spectra of CO stretching regions over Ni/SBA-15 plotted with time of temperature ramp from 303 K to 573 K.

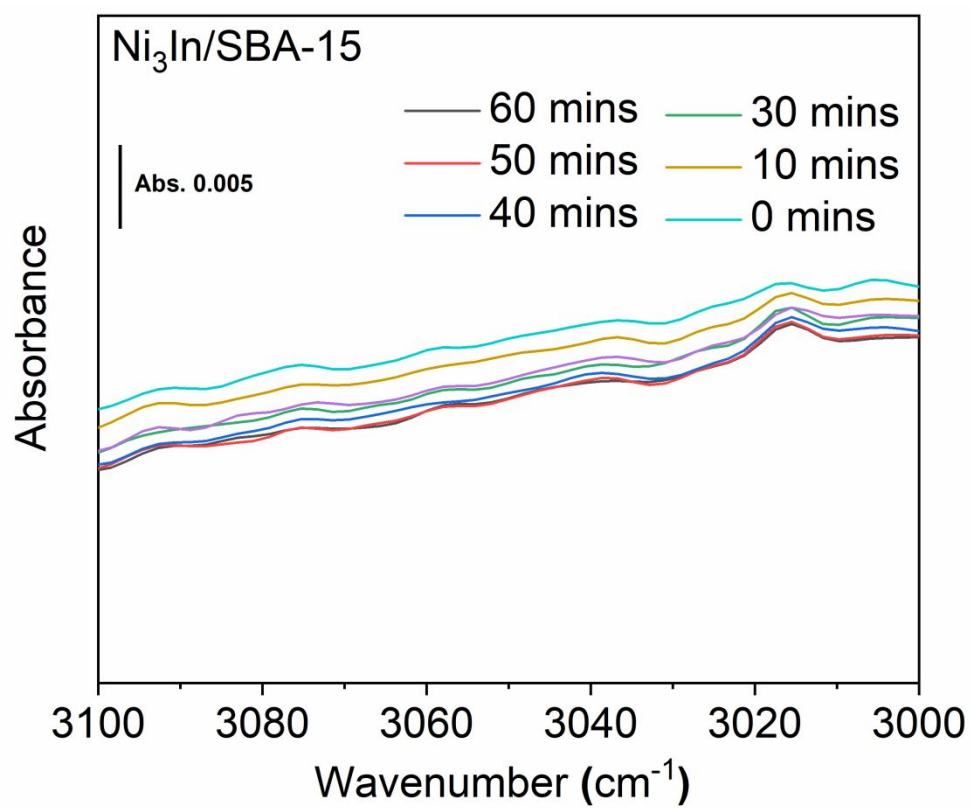


Figure S18. Successive DRIFTS spectra of CH_{str} stretching regions over Ni₃In/SBA-15 for an hour on stream.

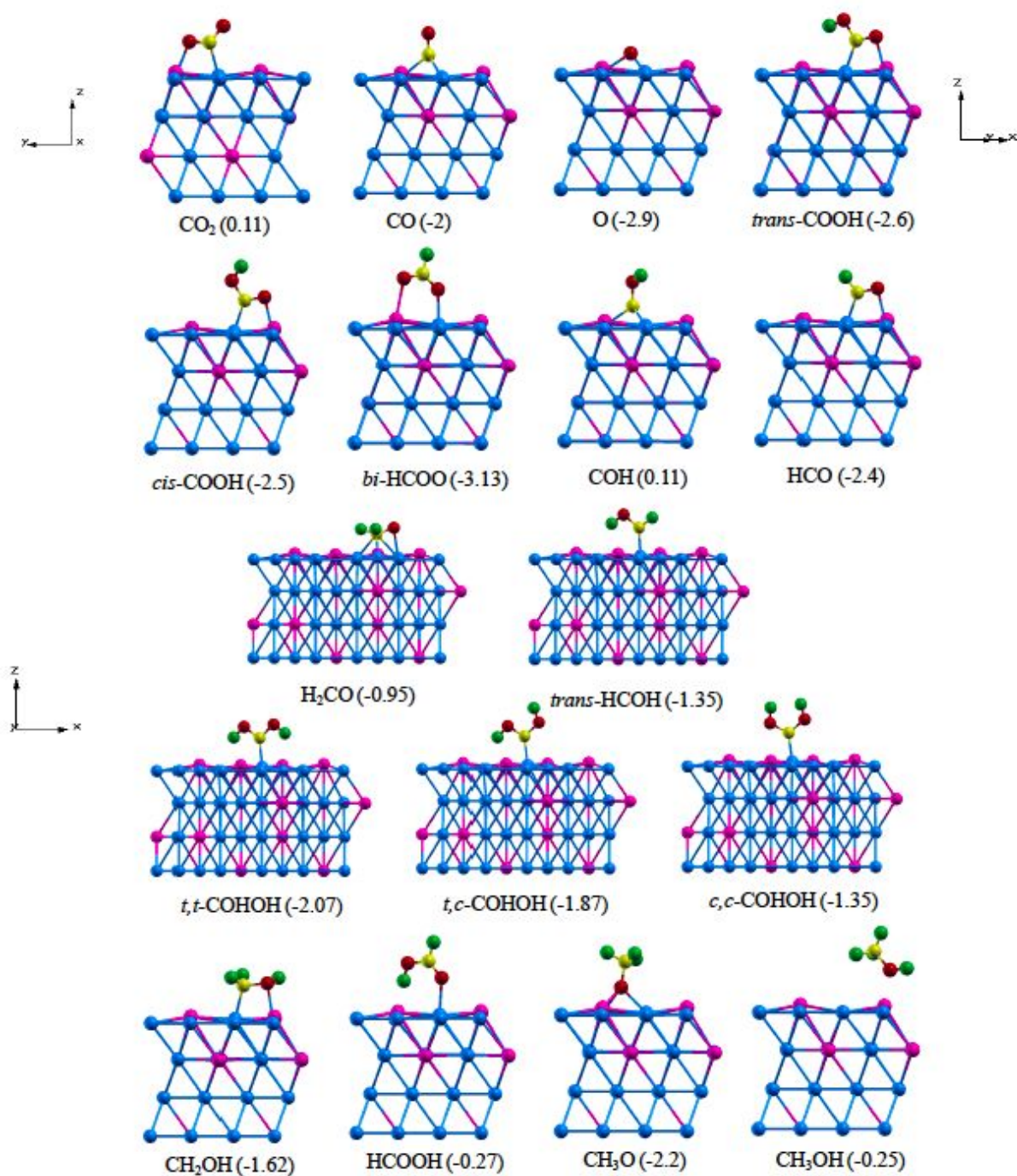


Figure S19. Optimized structures and binding energies of various intermediates occurring via various CO₂ hydrogen pathways on Ni₃In (111) surface. Magenta, blue, red, green and yellow spheres correspond to In, Ni, O, H and C atoms respectively. Binding energies are in eV.

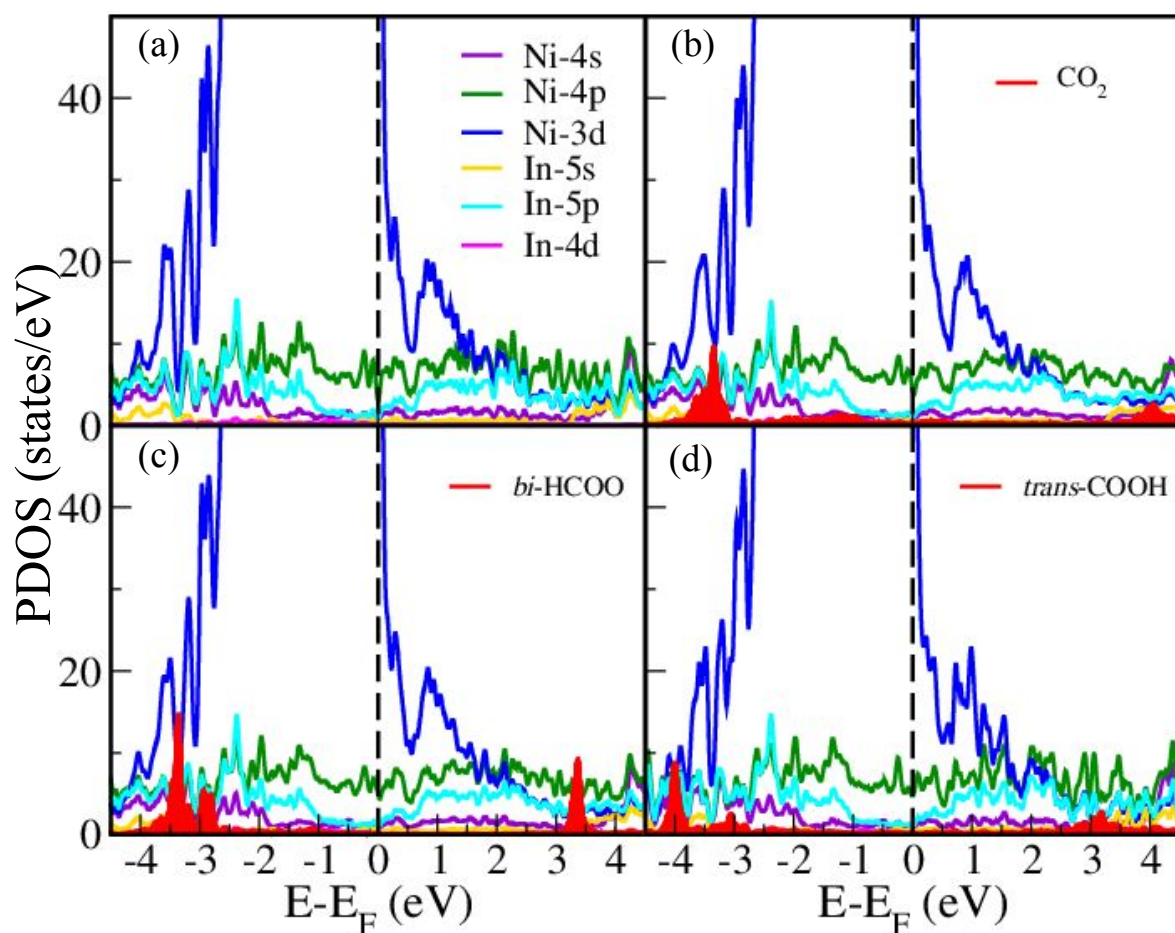


Figure S20. PDOS of (a) pristine Ni_3In (111) surface and (b) CO_2 , (c) *bi*-HCOO and (d) *trans*-COOH adsorbed on Ni_3In (111) surface. Dashed black line represents the Fermi energy.

References

1. Zhao, D.; Huo, Q.; Feng, J.; Chmelka, B. F.; Stucky, G. D., Nonionic triblock and star diblock copolymer and oligomeric surfactant syntheses of highly ordered, hydrothermally stable, mesoporous silica structures. *J. Am. Chem. Soc.* **1998**, *120* (24), 6024-6036.
2. Björk, E. M., Synthesizing and characterizing mesoporous silica SBA-15: A hands-on laboratory experiment for undergraduates using various instrumental techniques. *J. Chem. Ed.* **2017**, *94* (1), 91-94.
3. Studt, F.; Sharafutdinov, I.; Abild-Pedersen, F.; Elkjær, C. F.; Hummelshøj, J. S.; Dahl, S.; Chorkendorff, I.; Nørskov, J. K., Discovery of a Ni-Ga catalyst for carbon dioxide reduction to methanol. *Nat. Chem.* **2014**, *6*, 320.
4. Bourikas, K.; Kordulis, C.; Lycourghiotis, A., The role of the liquid-solid interface in the preparation of supported catalysts. *Catal. Rev.* **2006**, *48* (4), 363-444.
5. Grosman, A.; Ortega, C., Capillary condensation in porous materials. hysteresis and interaction mechanism without pore blocking/percolation process. *Langmuir* **2008**, *24* (8), 3977-3986.
6. Storck, S.; Bretinger, H.; Maier, W. F., Characterization of micro- and mesoporous solids by physisorption methods and pore-size analysis. *Appl. Catal. A* **1998**, *174* (1-2), 137-146.
7. Marakatti, V. S.; Peter, S. C., Nickel-antimony nanoparticles confined in SBA-15 as highly efficient catalysts for the hydrogenation Of nitroarenes. *New. J. Chem.* **2016**, *40* (6), 5448-5457.
8. Giannozzi, P.; Baroni, S.; Bonini, N.; Calandra, M.; Car, R.; Cavazzoni, C.; Ceresoli, D.; Chiarotti, G. L.; Cococcioni, M.; Dabo, I.; Dal Corso, A.; de Gironcoli, S.; Fabris, S.; Fratesi, G.; Gebauer, R.; Gerstmann, U.; Gougoussis, C.; Kokalj, A.; Lazzeri, M.; Martin-Samos, L.; Marzari, N.; Mauri, F.; Mazzarello, R.; Paolini, S.; Pasquarello, A.; Paulatto, L.; Sbraccia, C.; Scandolo, S.; Sclauzero, G.; Seitsonen, A. P.; Smogunov, A.; Umari, P.; Wentzcovitch, R. M., QUANTUM ESPRESSO: a modular and open-source software project for quantum simulations of materials. *J. Phys.: Condensed Matter* **2009**, *21* (39), 395502.
9. Vanderbilt, D., Soft self-consistent pseudopotentials in a generalized eigenvalue formalism. *Phys. Rev. B* **1990**, *41* (11), 7892-7895.
10. Perdew, J. P.; Burke, K.; Ernzerhof, M., Generalized Gradient Approximation Made Simple. *Phys. Rev. Lett.* **1996**, *77* (18), 3865-3868.
11. Henkelman, G.; Uberuaga, B. P.; Jónsson, H., A climbing image nudged elastic band method for finding saddle points and minimum energy paths. *J. Chem. Phys.* **2000**, *113* (22), 9901-9904.
12. Bavykina, A.; Yarulina, I.; Al Abdulghani, A. J.; Gevers, L.; Hedhili, M. N.; Miao, X.; Galilea, A. R.; Pustovarenko, A.; Dikhtiarenko, A.; Cadiau, A.; Aguilar-Tapia, A.; Hazemann, J.-L.; Kozlov, S. M.; Oud-Chikh, S.; Cavallo, L.; Gascon, J., Turning a methanation Co catalyst into an In-Co methanol producer. *ACS Catal.* **2019**, *9* (8), 6910-6918.
13. Tan, Q.; Shi, Z.; Wu, D., CO₂ hydrogenation to methanol over a highly active Cu-Ni/CeO₂-nanotube catalyst. *Ind. Eng. Chem. Res.* **2018**, *57* (31), 10148-10158.
14. García-Trenco, A.; Regoutz, A.; White, E. R.; Payne, D. J.; Shaffer, M. S. P.; Williams, C. K., PdIn intermetallic nanoparticles for the hydrogenation of CO₂ to methanol. *Appl. Catal. B* **2018**, *220*, 9-18.

15. García-Trenco, A.; White, E. R.; Regoutz, A.; Payne, D. J.; Shaffer, M. S. P.; Williams, C. K., Pd₂Ga-based colloids as highly active catalysts for the hydrogenation of CO₂ to methanol. *ACS Catal.* **2017**, 7 (2), 1186-1196.
16. Snider, J. L.; Streibel, V.; Hubert, M. A.; Choksi, T. S.; Valle, E.; Upham, D. C.; Schumann, J.; Duyar, M. S.; Gallo, A.; Abild-Pedersen, F.; Jaramillo, T. F., Revealing the synergy between oxide and alloy phases on the performance of bimetallic In–Pd catalysts for CO₂ hydrogenation to methanol. *ACS Catal.* **2019**, 9 (4), 3399-3412.
17. Shi, Z.; Tan, Q.; Tian, C.; Pan, Y.; Sun, X.; Zhang, J.; Wu, D., CO₂ hydrogenation to methanol over Cu-In intermetallic catalysts: effect of reduction temperature. *J. Catal.* **2019**, 379, 78-89.
18. Studt, F.; Sharafutdinov, I.; Abild-Pedersen, F.; Elkjær, C. F.; Hummelshøj, J. S.; Dahl, S.; Chorkendorff, I.; Nørskov, J. K., Discovery of a Ni-Ga catalyst for carbon dioxide reduction to methanol. *Nat. Chem.* **2014**, 6 (4), 320-324.